Journal of Electronic Materials (2025) 54:10164–10180
https://doi.org/10.1007/s11664-025-12386-5

ORIGINAL RESEARCH ARTICLE

CuI-Derived Cu_xO Thin Films Development via Thermal Oxidation for Lead-Free Perovskite Solar Cells

Md. Jakir Hossen[1,2] · Md. Shahinuzzaman[3,4] · M. S. Jamal[3] · Suhana Mohd Said[1,5] · S. F. W. M. Hatta[1,5] · Md. Helal Miah[6,7] · Mayeen Uddin Khandaker[6,8,9] · Mohammad Nur-E-Alam[10,11] · Mohammad Aminul Islam[1,5,12]

Received: 20 June 2025 / Accepted: 27 August 2025 / Published online: 18 September 2025
© The Author(s) 2025

Abstract

The development of low-cost, stable, and efficient hole transport layers (HTLs) is crucial to the advancement of lead-free perovskite solar cells. In this work, a solution-based oxidation process is employed to convert spin-coated copper iodide (CuI) films into mixed-phase copper oxide (Cu_xO) thin films comprising Cu_2O and CuO. Oxidation occurs under moderate temperatures (200–300°C), leading to uniform, compact, and highly conductive p-type films with tunable bandgaps. Structural, morphological, and optical analysis confirms successful phase transformation, and measurements of Hall effect reveal maximum mobility of holes of 26.7 $cm^2\ V^{-1}\ s^{-1}$ for double-coated films annealed at 300°C. Device simulations via SCAPS-1D using these measured properties predict that Cu_xO HTLs can make high-efficiency lead-free perovskite solar cells with $Cs_2AgBi_{1-x}Sb_xBr_6$ absorbers. While experimental device integration is yet to be demonstrated, this research lays the foundation for oxidized CuI-derived Cu_xO as a potential candidate inorganic HTL for green photovoltaics and offers thoughtful guidance for subsequent experimentation.

Keywords Spin coating · ambient oxidation · structural transformation · Cu_xO · double-halide PSCs · efficiency

✉ Mohammad Nur-E-Alam
m.nur-e-alam@ecu.edu.au

✉ Mohammad Aminul Islam
aminul.islam@um.edu.my

[1] Department of Electrical Engineering, Faculty of Engineering, Universiti Malaya, Jalan Universiti, 50603 Kuala Lumpur, Malaysia

[2] Department of Physics, Hajee Mohammad Danesh Science and Technology University, Dinajpur 5200, Bangladesh

[3] Institute of Energy Research and Development, Bangladesh Council of Scientific and Industrial Research (BCSIR), Dhaka 1205, Bangladesh

[4] Department of Electrical and Electronic Engineering, Uttara University, Dhaka 1230, Bangladesh

[5] Center of Printable Electronics, Universiti Malaya, Jalan Universiti, 50603 Kuala Lumpur, Malaysia

[6] Applied Physics and Radiation Technologies Group, CCDCU, Faculty of Engineering and Technology, Sunway University, 47500 Bandar Sunway, Selangor, Malaysia

[7] Department of Physics, Gopalganj Science and Technology University, Gopalganj, Dhaka 8100, Bangladesh

[8] Faculty of Graduate Studies, Daffodil International University, Birulia, Daffodil Smart City, Savar, Dhaka 1216, Bangladesh

[9] Department of Physics, College of Science, Korea University, 145 Anam-ro, Seongbuk-gu, Seoul 02841, Republic of Korea

[10] Centre for Promotion Research, Graphic Era (Deemed to be University), Clement Town, Dehradun, India

[11] School of Science, Edith Cowan University, 270 Joondalup Drive, Joondalup, WA 6027, Australia

[12] Miyan Research Institute, International University of Business Agriculture and Technology (IUBAT), Dhaka 1230, Bangladesh

Introduction

Perovskite solar cells (PSCs), known as a promising third-generation photovoltaic technology, have drawn significant attention due to their straightforward fabrication, cost-effectiveness, and impressive efficiency, which has surged from 3.8% to nearly 26.95% by attaining a deeper understanding of photo-physics, the optimization of device components, and controlling growth parameters.[1] In this advancement of the PSCs, hole transport layers (HTLs) play an essential role in effectively extracting holes and inhibiting electron transfer, with commonly utilized HTLs including Spiro-OMeTAD and PEDOT:PSS presenting inspiring performance.[2] However, generally, these organic HTLs are responsible for the initiation of degradation in the perovskite layers of a PSC device.[3] In addition, they present obstacles related to their high costs for organic synthesis and sophisticated fabrication processes (requiring complex air-sensitive processing steps).[4] More specifically, organic HTLs such as PEDOT:PSS can negatively impact the stability of perovskite materials owing to their high acidity due to its hygroscopic dopants. Moreover, Spiro-OMeTAD faces challenges related to stability and cost, which restrict its commercialization.

Nowadays, inorganic HTLs have emerged as viable alternatives owing to their robust chemical stability, facile fabrication approaches, and reduced costs. Materials including nickel oxide (NiO),[5] copper thiocyanate (CuSCN),[6] copper iodide (CuI), and copper oxide (Cu_xO)[7] exhibit promising optoelectronic properties which are essential for perovskite-based solar cells.[8] Ni-based HTL compounds may pose environmental and health risks due to nickel's carcinogenic classification. Among all materials, Cu_xO displays notable optoelectronic properties, including high charge carrier mobility, low electron affinity, and optimal band alignment with perovskites.[9] In addition, it can establish efficient ohmic contacts with its neighboring layers, thereby enhancing carrier transportation and device stability.[10] Cu_xO is considered a green and sustainable hole transport layer (HTL) due to its earth abundance and non-toxicity. Moreover, a number of simple straightforward and inexpensive conventional environmentally benign techniques can be used to create Cu_xO thin films,[11] including sequential ionic-layer adsorption and reaction (SILAR),[12] electrochemical deposition,[13] thermal oxidation,[14] chemical dissolution,[15] reactive dc sputtering,[16] sol-gel spin coating,[17] spray pyrolysis,[18] and metal-organic chemical vapor deposition.[19] Compared to NiOx, Cu_xO avoids the use of heavy metals and offers intrinsic p-type conductivity with favorable energy-level alignment for efficient hole extraction.[12] These features collectively make Cu_xO a promising green alternative for scalable and sustainable perovskite solar cell development. Cu_xO as an inorganic HTL has several benefits to the perovskite-based solar cell; however, maximum efficiency with CuO-based p-i-n structure of Pb-halide perovskite was only reported at 17.1%,[20] which is much lower than the efficiency attained with organic HTL. This suggests that more research is necessary to enhance efficiency.[10] It has also been reported that, in 30% humidity, unmodified Cu_2O retained 80% original efficiency after 30 days, and modified Cu_2O retained 90% original efficiency after 30 days, whereas Spiro-OMeTAD retained only 50% after 30 days.[10] This paper presents a cost-effective method for producing nanoscale CuO-Cu_2O mixed thin films through a one-step solution-processed spin coating technique for application as HTL in a PSC. The structural and optical characterization of these films was performed by cutting-edge methods, including x-ray diffraction (XRD), field-emission scanning electron microscopy (FESEM), energy-dispersive spectroscopy (EDS), UV–visible–near-infrared (NIR) spectroscopy, Fourier transform infrared (FTIR) spectroscopy, and Hall effect measurement. In addition, the impact of the number of deposition/coatings, temperature variation, and variations in annealing time on optoelectronic properties was analyzed. Finally, utilizing the experimental optoelectronic properties of CuO-Cu_2O mixed thin film in n-i-p structured fluorine tin oxide (FTO)/ZnOS/$Cs_2AgBi_{1-x}Sb_xBr_6$/Cu_xO/Au, a theoretical investigation was conducted using SCAPS-1D solar cell simulator software. This is a less explored non-toxic and easily fabricated absorber material for the application of PSCs, which may decrease the production expenditure.[21] Sb doping with Cs2AgBiBr6 material reduces the bandgap up to 2.22-1.86 eV and enhances stability with humidity levels of 30–50% for about 120 days as an active absorber layer for PSCs.[22] Very good crystallinity was reported by Yuan et al. in 2019[23] which is also compatible with other layers (HTL and ETL) with their bandgap alignment.[24] In addition, the parameters for each individual layer have been optimized for their role in the performance of the device. We believe that the experimental and theoretical methods used in this study will yield important insights that will open the door for the production of high-efficiency halide double-PSCs in the solar industry.

Experimental Methods

Materials and Thin Film Preparation

The precursor solution was prepared by all analytical grade chemicals, which were purchased from different suppliers. Copper(I) iodide 99.5% and acetonitrile (CH_3CN) 99.9% Chromasolv gradient grade were purchased from

Sigma-Aldrich, USA. Acetone, piranha solution (sulfuric acid (H_2SO_4), and hydrogen peroxide (H_2O_2)) were purchased from Merck, Germany. All commercially available chemical reagents were used directly after delivery without further purification.

A total of 150 mg CuI was mixed with 5 mL of acetonitrile to make a precursor solution. Then the solution was stirred with a magnetic stirrer for about 10 min at 60°C. The glass substrates were first cleaned with piranha solution to dispel the gross contaminants. Then the glass substrates were cleaned with acetone and distilled water and dried with an air blower before film deposition. The precursor solution was then spin-coated at 500 rpm for 10 s and 3000 rpm for 60 s on the glass substrate. The process was repeated to fabricate thin films with various thicknesses. Then it was annealed at 110°C for further crystallization for all samples for 10 min. After that, the thin film was annealed at different annealing temperatures (110°C, 250°C, 300°C, 350°C) for 30 min. CuI can react with O_2 and form CuO after heating at 250°C in air. All experiments were carried out with ambient temperature at ~ 25 ± 2°C, relative humidity about ~ 45 ± 5%, atmospheric pressure close to 1 atm, and oxygen concentration in the ambient environment ~ 20.9%. Device optimization was conducted by SCAPS-1D software using the experimental data of the prepared HTL thin films.

Characterization Studies

Different cutting-edge analytical instruments including an X-ray diffractometer (Drywell XRD-7000, CuKα (λ = 1.54178 Å) radiation, and a Fourier transform infrared (FTIR) spectrophotometer (PerkinElmer Spectrum Two, wavenumber range 8300–350 cm^{-1}) were used for this research work. Electrical characteristics such as resistivity, carrier concentration, and carrier mobility were measured using a van der Pauw variable temperature Hall effect measurement system (Ecopia HMS-3000, NO ID ASET: HO36502). The optical properties (absorbance and optical bandgap) of these synthesized thin films were investigated using a UV/Vis spectrometer (SPECORD 200 PLUS-223E1128F, Analytik Jena, Germany) in the wavelength range of 200–800 nm. The optical bandgap value (E_g) of the films can be computed through extrapolation of the $(\alpha h\nu)^2$ versus hν curve since photon energy is E_g when $(\alpha h\nu)^2$ becomes zero. For that purpose, the value of the optical absorption coefficient (α) is calculated using film thickness, transmittance, and reflectance data using a mathematical correlation between these parameters. For FESEM analysis, the Cu_xO thin films were first gold (Au)-coated before being introduced into the FESEM chamber, and then their overall morphology was determined using an accelerating voltage of 5–10 kV. The qualitative elemental analysis was carried out using an EDS system attached to an FESEM instrument. SCAPS-1D software was used to observe the solar cell performance of Cu_xO as an HTL from the data experimentally mined from this study.

Results and Discussion

Structural Properties

The structural characteristics of Cu_xO thin films as ascertained by XRD are displayed in Fig. 1. At 110°C, single-coated film shows strong peaks at 25.6° and 52.6°, which indicates a CuI layer with (111) and (222) *hkl* planes according to the ICDD card no. 00-006-0246. At an annealing temperature of 250°C, the single-coated film starts to crystallize as CuO with fewer weak peaks for the (002), (111), and (202) *hkl* planes at points 35.7°, 39°, and 59.5°, respectively, which is supported by the ICDD card no. 01-088-8871. A similar pattern with small, prominent peaks was seen at 35.5° and 38.7° for annealing temperatures of 300°C and 350°C, respectively. This resulted from the migration of oxygen into the films, induced by the conversion of Cu_2O.

The films fully convert to CuO when the sample is annealed at 300°C. Annealing at 350°C maintains the CuO composition.[25] Cu_2O begins to react with oxygen, forming the CuO phase in the process: $2Cu_2O + O_2 \rightarrow 4CuO$. Based on thermodynamic principles, the reaction's Gibbs free energy at approximately 250°C is approximately −3.73 kcal mol^{-1}. Consequently, this reaction provides an easy explanation for the CuO phase development at 300°C.[26] Conversely, for the double-coated film, when annealed at 110°C and 250°C, the film remains in the CuI phase according to the ICDD card no. 00-006-0246. However, at 300°C and 350°C, films exhibit CuO phase according to ICDD card no. 01-088-8871. For double-coated film, the phase only starts to change after 250°C annealing temperature. Hence, for annealing at 250°C and 300°C both CuO and Cu_2O phases were present in the sample.

The structural calculation (crystallite size D, d-spacing, microstrain (ε), dislocation density (δ)) summary is shown in Table I. Scherrer's equation, $D = 0.9\lambda/\beta\cos\theta$, was used to calculate the crystallite size, where θ is the Bragg diffraction angle, β is the full width at half maximum (FWHM) in radians, D is the average crystallite size, and λ is the X-ray wavelength (1.5406 Å for the CuKα line). The calculation was done using the FWHM of the main peak among the all peaks. Cu_xO (x = 1,2) and CuI crystal sizes range from 41.25 nm to 80.60 nm, which increases with the increase in the number of depositions, resulting in larger grain sizes. This observation is consistent with the XRD peaks' increased constriction. A thinner peak indicates a greater crystallite size and fewer crystal defects, according to kinematic scattering theory. The

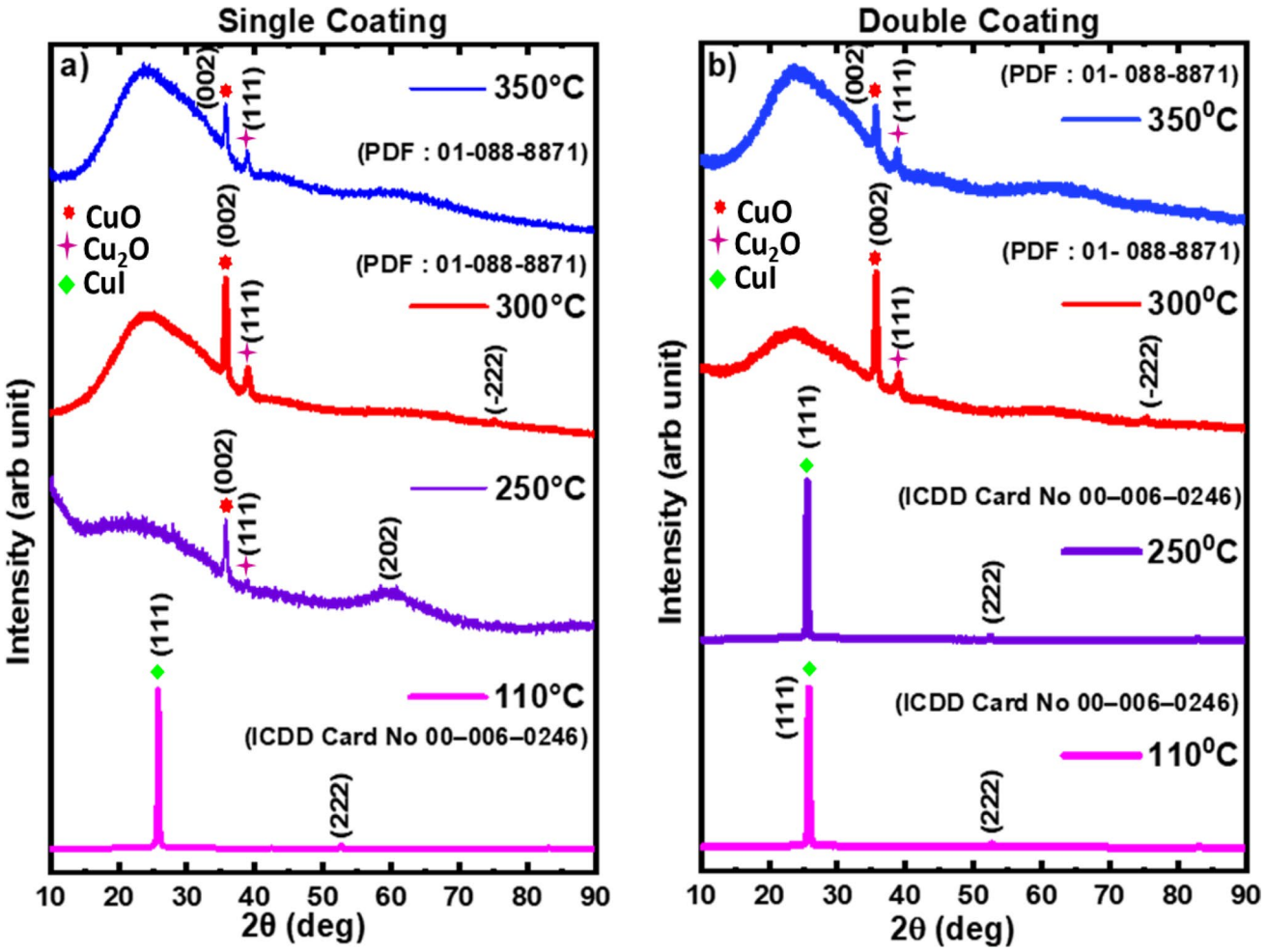

Fig. 1 XRD peak of (a) single-coated film and (b) double-coated film annealed at 110°C, 250°C, 300°C, and 350°C for 30 min each sample.

Table I Calculated crystal structural information of single- and double-coated thin films at different annealing temperatures for about 10 min

Deposition	Annealing temp.	*hkl* plane	2θ (°)	FWHM β (radians) x 10^{-3}	Crystallite size D (nm)	d-spacing (Å)	Microstrain (ε) (10^{-4})	Dislocation density (δ) (10^{14}/m^{-2})
Single coating	110°C	(111)	25.6	1.744	80.57 ± 0.015	3.486	19.2	1.54
	250°C	(002)	35.7	3.489	41.27 ± 0.045	2.512	27.09	5.87
	300°C	(−111)	35.7	2.617	55.03 ± 0.027	2.512	20.31	3.30
	350°C	(−111)	35.7	3.489	41.27 ± 0.012	2.512	27.09	5.87
Double coating	110°C	(111)	25.8	1.744	80.60 ± 0.031	3.449	19.04	1.54
	250°C	(111)	25.6	1.744	80.57 ± 0.041	3.475	19.20	1.54
	300°C	(−111)	35.7	2.617	55.03 ± 0.018	2.512	20.31	3.30
	350°C	(−111)	35.6	3.489	41.26 ± 0.013	2.519	27.17	5.87

interplanar spacing can also be computed using Bragg's equation, $d = n\lambda/2\sin\theta$, in which n is an integer, θ is the Bragg diffraction angle, and λ is the X-ray wavelength (1.5406 Å for the CuKα line).[27] The d-spacing decreases with the increase in the annealing temperature for both single- and double-coated films due to the shrinking in the crystallite size. It is important to remember that interstitial atoms are linked to microstrain and lattice distortion, which in turn affect crystal deformation. The microstrain causes the XRD lines to broaden without changing the

peak position. The calculation involves determining the root mean square of the fluctuations in the lattice parameters across the entire sample. It can be calculated by $\varepsilon = \beta / 4\tan\theta$. The dislocation density expresses the defects per unit volume and vacancies, which can be determined by the relation $\delta = 1/D^2$. The larger dislocation density was observed at 250°C and 350°C for single-coated films and for double-coated films at 350°C annealing temperatures. Hence, the lower dislocation density represents the low defect and better optoelectrical performances. At 250°C, the lowest dislocation density was observed for double-coated film. However, for both single-coated and double-coated films, the change in annealing temperature is evident in the microstrain and dislocation density alteration. The atomic ratios of $Cu^{x+}(x = 1,2)$ and O^{2-}, which can result in interstitial defects, may have been responsible for it. Additionally, as indicated in Table I, peak shifting was also noted for the various Cu_xO layers. This suggests that the interlayer distance varied as a result of the partial replacement of Cu^{x+} and O^{2-} atoms in their reference lattice during the deposition and thermal annealing processes.

FESEM and EDS

The FESEM image for Cu_xO thin films with varying annealing temperatures and coating numbers after 30 min is displayed in Fig. 2. An important factor influencing the microstructure of the films is the annealing temperature. Figure 2a shows that the film, when it is formed (annealing temperature of 110°C), has an uneven grain size and a rough mesoporous surface for both single and double-coated films.

The film annealed at 250°C shows a consistent smooth and regular granular film compared to the surface of films annealed at 110°C as observed in Fig. 2b. However, the grain size for the single-coated film is 48.63% smaller than the double-coated film for the film annealed at 250°C. When copper oxide was annealed at 300°C, the FESEM image revealed dense, spherical formations with no obvious defects. The grain size of the film annealed at 300°C was larger than even the grain size of the film annealed at 350°C from Fig. 2c, as this time it was completely changed to CuO. The haphazard distribution of grains, in projection and size, only suggests a random orientation of isotropic and smooth grains.[28]

Figure 3a shows that the copper and oxygen percentages for the film annealed at 250°C were approximately 53.99% and 25.89%, respectively. In contrast, the oxygen percentage rose to 33.79% for the film annealed at 300°C as can be seen in Fig. 3b. This indicates the film's crystal transformation as a result of annealing in ambient conditions.

Fourier Transform Infrared (FTIR) Spectroscopy

FTIR measurements are employed to identify vibrational signatures of functional groups (e.g., C–H, N–H, C−O, S−O) in perovskite solar cell components, enabling analysis of chemical bonding, film formation, interfacial interactions, and degradation mechanisms such as solvent coordination or moisture-induced decomposition. In this study, FTIR was specifically used to confirm the formation of Cu_xO phases and to assess the compositional characteristics of the deposited thin films, which are critical for device stability and performance. Thin films annealed at temperatures of 110°C, 250°C, 300°C, and 350°C were measured using FTIR analysis for single and double coatings. Table II represents the FTIR data and their corresponding bond stretching. Figure 4 provides the FTIR absorbance spectra of thin layers of Cu_xO deposited on a glass substrate in the range of 400–4000 cm^{-1} with single and double coatings by varying the number of annealing temperatures.

It has been noted that the creation of CuI is preferred at oxidation temperatures up to 250°C, while CuO is formed at higher temperatures. This outcome shows a strong correlation with the XRD measurements of the CuI (111) peak's appearance and increasing intensity. Moreover, we observed a strong CuO peak at 487 cm^{-1} for the single coating for annealing temperatures of 300°C and 350°C.[25] In the case of double-coated film for annealing temperatures of 300°C and 350°C, there is a noticeably strong band at 495 $cm^{-1,}$ which confirmed the presence of CuO thin film, whereas at 250°C there is no observable peak.[29] This indicates that at 250°C, CuI film forms in the thin film. More specifically, an absorption band of Cu_2O at about 603 cm^{-1} is detected for temperatures up to 250°C. In addition, Cu–O stretching of Cu_2O is linked to the strong peak at 610 cm^{-1}.[30,31] Nevertheless, the creation of CuO near the surface as a result of post-deposition oxidation in the atmosphere, which is known to occur for Cu_2O films, is a more likely explanation. In other words, the absorbance percentage corresponding to the Cu–O bond stretching increases as the annealing temperature is increased, suggesting a more noticeable production of cupric oxide at higher temperatures. A significant difference can be seen in FTIR patterns for single-coated and double-coated films. In double-coated films, the number of peaks, even some of which are unrecognized, is increased; the cause of the phenomena is yet to be explored.

As can be seen in the figure, other peaks are observed at 1083 cm^{-1} for single-coated film, and 1108 and 1261 cm^{-1} for double-coated film. The peak at 1592 cm^{-1} is attributable to C–O stretching vibration bonds. Peaks at 1465, 1482, 1573, and 1708 cm^{-1} can be attributed to C–H and C=O stretching vibration bonds, respectively, and peaks at 2362 and 2372 cm^{-1} represent C=N stretching vibration bonds. No additional peaks were found in the

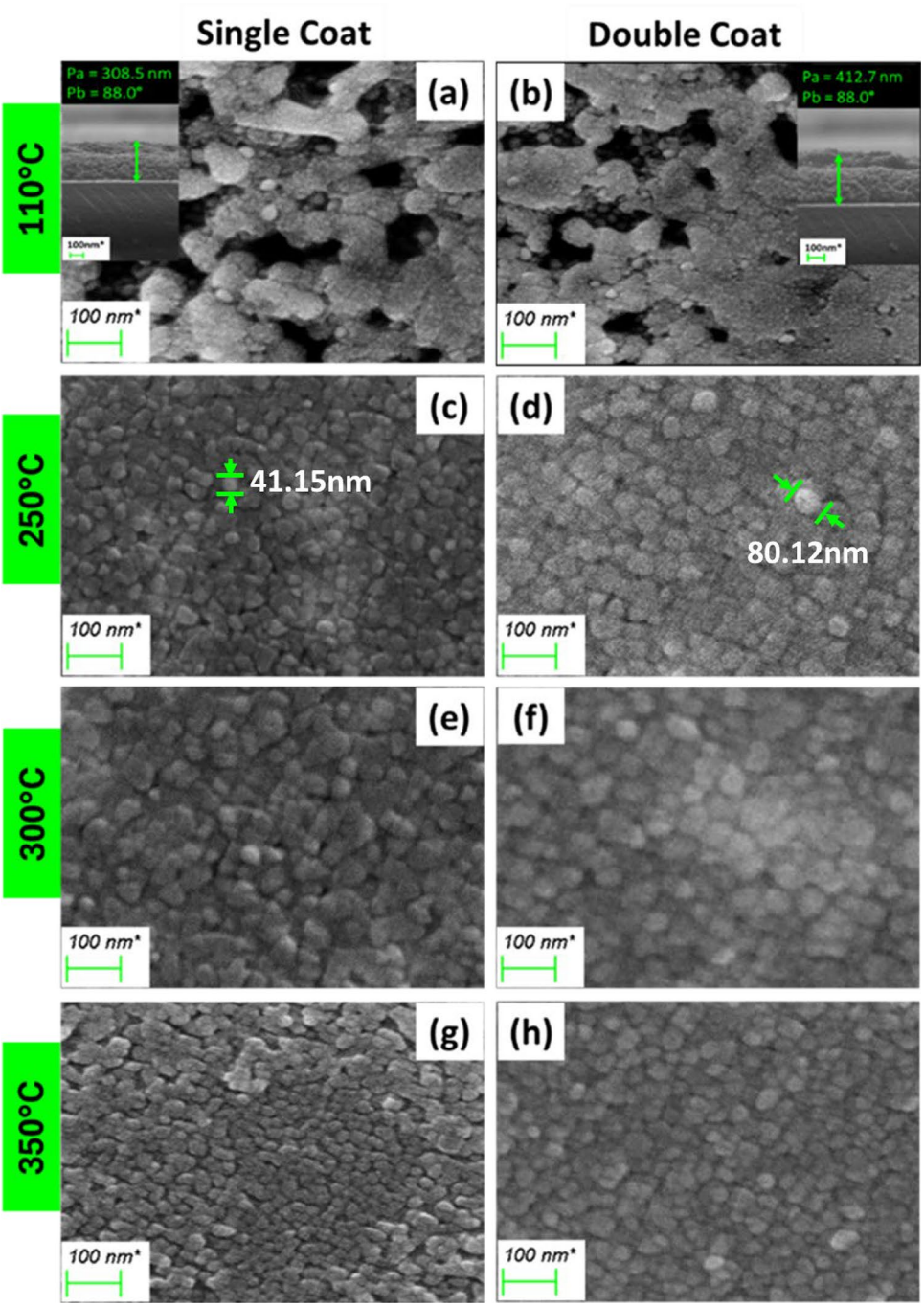

Fig. 2 FESEM image for the Cu_xO thin films: (a, b) 110°C, (c, d) 250°C, (e, f) 300°C, and (g, h) 350°C for single- and double-coated films, respectively (inset picture from Fig. 2a and b represents the cross-sectional view of single- and double-coated films).

2400–4000 cm^{-1} range, so they are not depicted in the image.[32] When the thickness increases, the intensity of these peaks also increases, suggesting that these groups are not at the surface but rather in the bulk of the film. Extending the pulse times of the reactant or precursor could perhaps rectify this incomplete exchange. Additional bands corresponding to C–O stretching, C–H bending, and C=O, C=N, and O–H stretching (in cm^{-1}) may correspond to adsorbed atmospheric gases.[33] Nevertheless, their magnitude, which is at the instrument's noise limit, prevents the extraction of reliable results.

Optical Properties

Figure 5 shows the UV-Vis transmission spectrum for single-layered and double-layered Cu_xO films using different annealing temperatures. For single-coated film, it was observed that transmission increases with the increase in

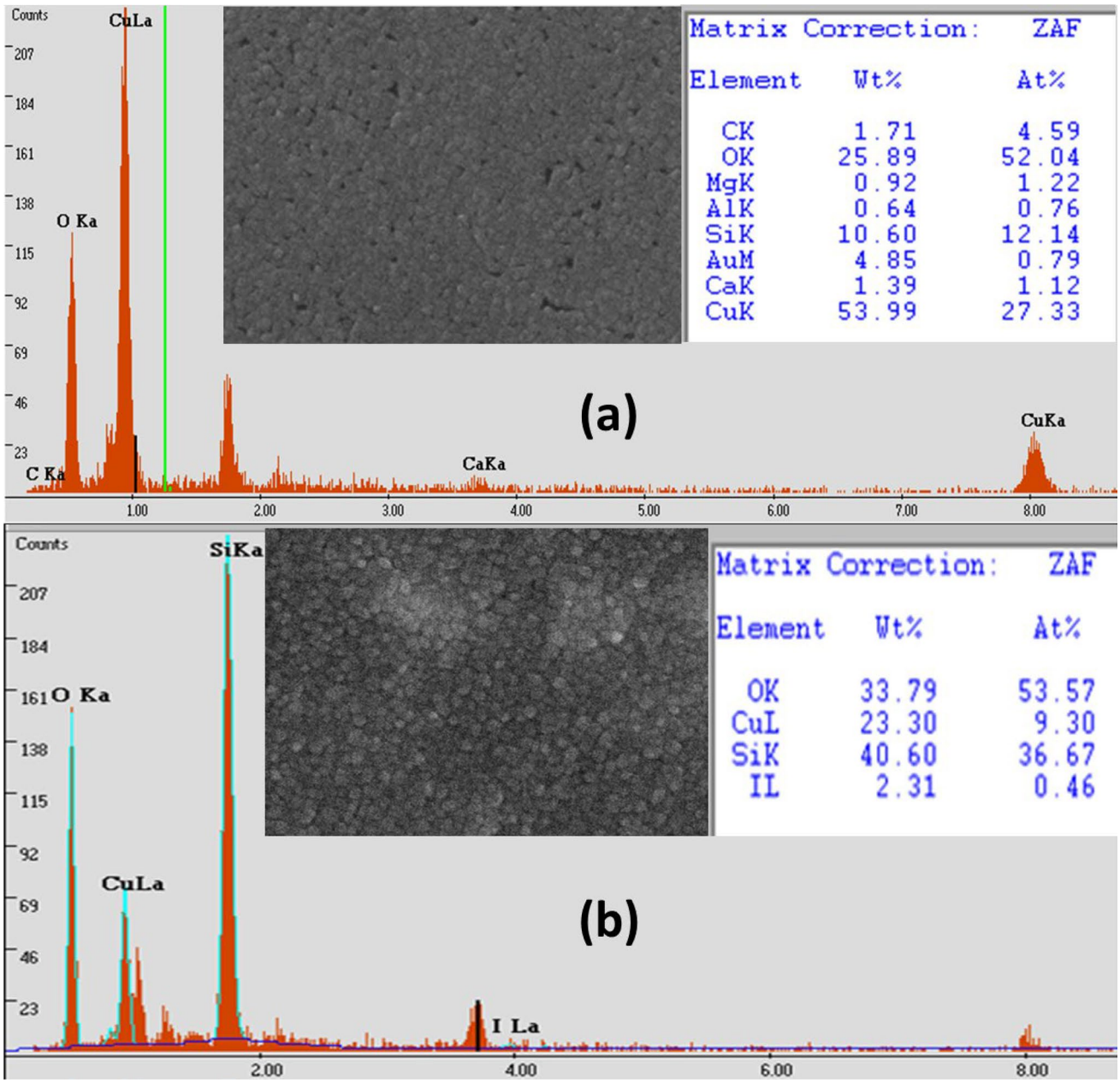

Fig. 3 EDS micrograph of Cu_xO thin films: (a) 250°C, (b) 300°C for single- and double-coated films, respectively. (Inset: corresponding film formation and elemental percentage).

annealing temperature. The lowest and highest transmission spectra occurred at 110°C and 350°C annealing temperatures, respectively. From wavelengths in the range of 200–300 nm, lower transmission spectra were observed for single-coated film compared to the visible-range spectra. All transmission spectra gradually increased at higher wavelengths relative to lower wavelength.

Nonetheless, it is noted that the pattern suggests a modest increase in transmission intensity with the increase in the number of layers. This may be explained by the fact that as the number of layers increases, so does the exposed surface area and, in turn, the thickness of the film. The lowest transmission was found for film annealed at 110°C in the visible range, whereas below 400 nm, the lowest transmission was observed for film annealed at 300°C. However, in the wavelength range of 300-350 nm, there is a sharp absorption peak observed for film annealed at 110°C and 300°C. The reason for these sharp peaks is unknown. High transmittance (low absorbance) in the

Table II FTIR data with corresponding bond stretching

CuO stretching	Single coating wavenumber (cm^{-1})	Double coating wavenumber (cm^{-1})
Cu–O stretching of CuO	487	495
Cu–O stretching of Cu_2O	603	610
O–H	767, 902,	754, 877
C–O	1083,	1108, 1261
C–H bending	1573	1465, 1482
C−O	–	1708
C−N	2362	2372

UV-Vis range is required for photons to readily flow through the HTL and be absorbed by the perovskite absorber.

Determining the optical bandgap can also demonstrate the phase change from Cu_2O to CuO. The optical absorption coefficient (α) was evaluated using the relation: $\alpha h\nu = A(h\nu - Eg)^{1/2}$, where A is a material-dependent constant, $h\nu$ is the photon energy, and E_g represents the optical bandgap. Following the method proposed by Roth, the Tauc plot of $(\alpha h\nu)^2$ versus $h\nu$ was constructed, as shown in Fig. 5c and d. The optical bandgap E_g was obtained by extrapolating the linear region of the $(\alpha h\nu)^2$–$h\nu$ curve to intersect the photon energy axis. The optical bandgap of the films as they are fabricated and annealed at 250°C and 300°C is almost the same, 2.20 eV and 2.22 eV, for double-coated film, whereas it is 2.87 and 2.78 eV for single-coated film. This is due to the mixed phase present in the sample which supports the XRD results. Hence, this ensures that mixed phases of Cu_xO (Cu_2O and CuO) are also present in the sample for 250°C and 300°C. After annealing at 300°C, all samples present CuO as a predominant phase. However, all samples have a bandgap of more than 2.0 eV which represents the Cu_2O phase present in the sample, which is in good agreement for application as an

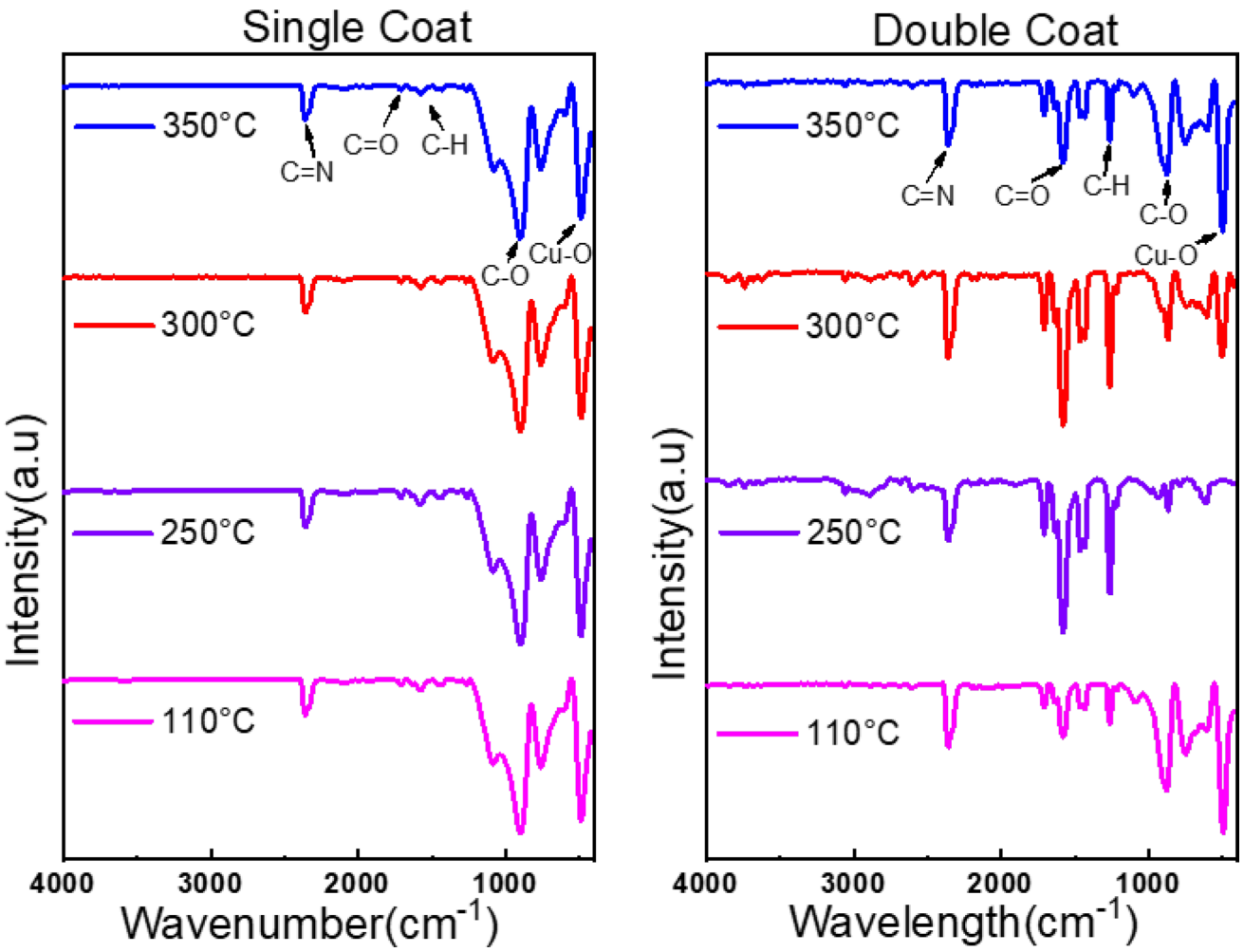

Fig. 4 FTIR absorbance spectra of Cu_xO single- and double-coated thin films for 110°C, 250°C, 300°C, and 350°C annealing temperatures.

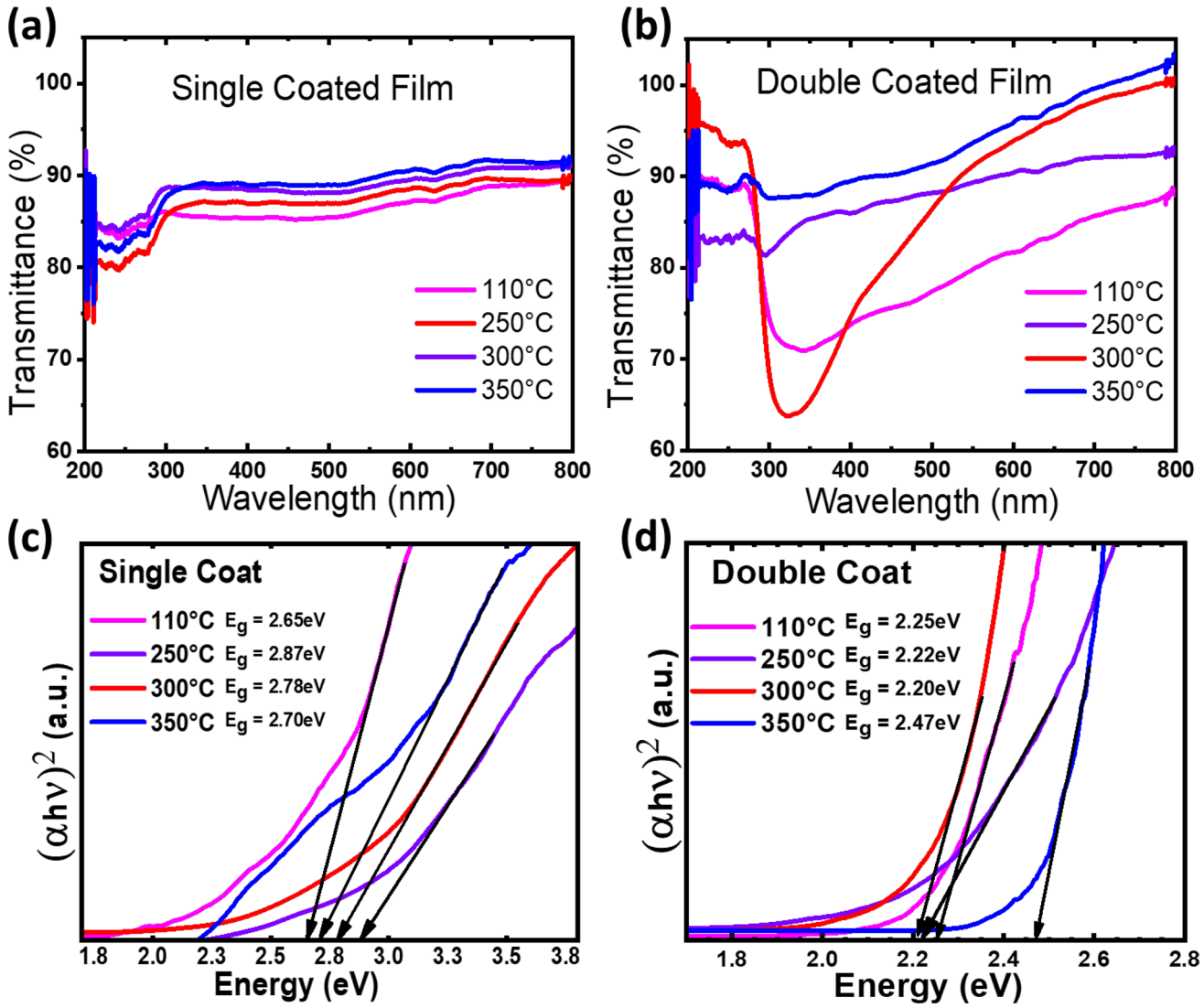

Fig. 5 (a-b) UV-vis transmittance for single-coated and double-coated thin films, (c-d) Bandgap calculation for single-coated and double-coated films at 110°C, 250°C, 300°C, and 350°C annealing temperatures, respectively.

HTL for better performance.[25] For annealing temperature of 350°C, the largest bandgap observed is about 2.47 eV for the double-coated film compared to films annealed at other temperatures. This is probably due to reducing the crystallinity (as shown in Fig. 1 and Table I) which may increase the bandgap as well. The higher annealing temperature also induces pores in the thin film (as shown in Fig. 2). Double-coated film for 300°C annealing temperature has a bandgap of 2.20 eV, which is in good agreement for the simulation results obtained (18.18% power conversion efficiency [PCE]) by Sing et al. in 2021.[34] Hence, in this work, this bandgap has been used to simulate the HTL performances for perovskite solar cells, which shows better performance (25.61% PCE) than the previous literature.

Hall Measurements

Table III below provides an overview of the copper oxide films' crystalline structure, bandgap energy, resistivity, carrier concentration, and mobility.

The findings demonstrate that the annealing temperature and number of depositions alter the copper oxide films' crystal structure, bandgap, resistivity, carrier concentration, and mobility. At 110°C annealing temperature for both single- and double-coated film a CuI structure formed according to the XRD and FTIR results. The carrier concentration of single-coated film annealed at 110°C was 1.39×10^{15} cm^{-3} and the resistivity was 1.27×10^{3} Ω-cm, which implies a carrier mobility of 2.95 cm^2V^{-1} s^{-1}, which is quite low. On the other hand, at same annealing temperature for double

Table III Hall measurements for Cu_xO thin films

No. of coatings	Variation of samples	Concentration (n) cm^{-3})	Mobility (μ) (cm^2/V s)	Resistivity (ρ) (Ω-cm)	Bandgap (E_g) (eV)
Single coat (annealing time 30 min)	110°C	1.39E+15	2.95	1.27E+03	2.65
	250°C	1.74E+15	5.31	4.32E+04	2.87
	300°C	1.73E+14	19.53	1.85E+03	2.78
	350°C	6.03E+14	17.25	6.00E+03	2.70
Double coat (annealing time 30 min)	110°C	1.39E+16	8.46	5.30E−01	2.25
	250°C	2.91E+15	24.66	6.51E+02	2.22
	300°C	5.30E+14	26.72	3.88E−01	2.20
	350°C	6.78E+14	24.39	1.21E+02	2.47

coating, the mobility (8.46 cm^2V^{-1} s^{-1}) observed was higher than for the single-coated film. This is due to a low resistivity of 5.30×10^{-1} Ω-cm; however, the carrier concentration (1.39×10^{16} cm^{-3}) was 90% higher than for the single-coated thin film carrier concentration (1.39×10^{15} cm^{-3}). At 250°C annealing temperature for single-coated film, the structure transformed from CuI to Cu_xO phase. However, for double-coated film it remains in the CuI phase. This is because the thickness is greater than that of the single-coated films which needed extra heat to change phase. After 250°C annealing temperature for both single and double coatings, the thin film's carrier mobility increased for single-coated film from 5.31 to 19.53 cm^2V^{-1} s^{-1} and from 24.66 to 26.72 cm^2V^{-1} s^{-1} for double-coated film. The film's carrier concentration decreased from 1.74×10^{15} to 1.73×10^{14} cm^{-3} and 2.91×10^{15} to 6.78×10^{14} cm^{-3} for single- and double-coated films, respectively, which can be explained by the decrease in crystal defects and the enhancement of crystal quality.

For the films annealed at 250°C and 300°C, the resistivity trend is nearly identical due to an increase in carrier mobility and a decrease in carrier concentration. At 300°C, the films changed into CuO crystals, causing the carrier concentration to increase. On the other hand, the data indicate that the film's carrier mobility increases as the carrier concentration decreases. This is because the decrease in carrier concentration will decrease carrier scattering and cause the carrier mobility to increase. At 350°C, the mobility slightly decreases about two units for each film as the resistivity increases from 1.85×10^{3} to 6.00×10^{3} Ω-cm and 3.88×10^{-1} to 1.21×10^{2} Ω-cm for both single- and double-coated films. Because of the intrinsic potential of the space-charge area, photogenerated electron-hole pairs in the thin films can separate more easily. However, the carrier concentration remains almost the same as for the annealing temperature of 300°C. Overall, we observed the highest carrier mobility 19.53 cm^2V^{-1} s^{-1} for single-coated thin film s and 26.72 cm^2V^{-1} s^{-1} for double-coated thin films. The reason behind the higher mobility at an annealing temperature of 300°C is because the surface becomes disturbed (mesoporous type) by the higher annealing temperature. Compared to conventional HTLs such as Spiro-OMeTAD (~10^{-4}–10^{-3} cm^2 V^{-1} s^{-1}, undoped) and PEDOT:PSS (~0.1–1 cm^2 V^{-1} s^{-1}), Cu_xO offers significantly enhanced hole mobility, enabling efficient charge extraction and reduced recombination losses. Cu_2O-based HTLs can exhibit mobilities between 10 and 30 cm^2 V^{-1} s^{-1}; however, their long-term stability can be affected by photoinduced and thermal oxidation (Cu^+ to Cu^{2+}), which degrades transport properties. Additionally, unencapsulated devices are susceptible to moisture-induced degradation of Cu_xO films. Thus, while the high mobility is advantageous, ensuring operational stability requires effective encapsulation and interface optimization strategies. Finally, carrier mobility 26.72 cm^2V^{-1} s^{-1} for double-coated thin films was used for simulation, which resulted in higher a PCE (25.45%) by SCAPS-1D software.

Device Simulation and Optimization

For the validation of experimental results, SCAPS-1D simulation software was used. SCAPS-1D is a highly efficient and user-friendly solar cell simulator, outperforming other tools such as COMSOL, Silvaco, and AMPS.[35,36] It can simulate up to seven different layers in a heterostructure system and operate under various ambient conditions, consistently aligning well with experimental results.[37] SCAPS-1D operates using three fundamental equations: Poisson's equation and the continuity equations for electrons and holes, referred to as Eqs. (1–3).[35]

$$\nabla^2 V = -\frac{q}{\epsilon}\left(p - n + N_D - N_A\right) \tag{1}$$

$$\nabla . J_p = q(G - R) \tag{2}$$

$$\nabla . J_n = q(R - G) \tag{3}$$

Solving these equations allows for the calculation of various parameters, including the energy band, defect density, doping concentrations, AC characteristics, and spectral response. The general equations for (2) and (3) are expressed as,

$$G(x) = \int_0^\infty \phi\alpha e^{-\alpha x} d\lambda \tag{4}$$

The current densities due to holes and electrons can be attained by using equations (2) and (3), and can be expressed as follows,

$$J_p = -q\mu_p p\nabla V_p - kT\mu_p \nabla_p \tag{5}$$

$$J_n = -q\mu_n n\nabla V_n + kT\mu_n \nabla_n \tag{6}$$

where

$$V_p = V - (1-\gamma)\Delta G/g \tag{7}$$

$$V_n = V + \gamma\Delta G/g \tag{8}$$

Here, p denotes hole concentration, n denotes electron concentration, V denotes electrostatic potential, q represents electric charge, ϵ represents permittivity, N_D represents donor density, N_A represents acceptor density, J_p represents current density due to holes, J_n represents current density due to electrons, V_p denotes the effective potential for holes, V_n denotes the effective potential for electrons, G represents generation rate, R represents recombination rate, μ_p represents the mobility of holes, μ_n represents the mobility of electrons, ΔG represents the variation in the band structure, and γ accounts for Fermi-Dirac statistics (Table IV).

Influence of Thickness

The absorber material plays a pivotal role in perovskite solar cells (PSCs), where thickness is a critical determinant of the device's efficiency.[43] The impact of absorber thickness on device performance was explored by varying the thickness of the absorber layer from 300 nm to 1500 nm while maintaining ETL and HTL at their optimized thicknesses (shown in Fig. 6). The photovoltaic parameter of current density (J_{SC}) experienced a 23.02% increase from its initial value. However, due to the change in absorber layer thickness, the fill factor (FF) and open-circuit voltage (V_{OC}) decreased from 90.14% to 89.76% and from 1.48 volts to 1.46 V, respectively. With lower thickness values, longer-wavelength photons exhibit low absorption, whereas shorter wavelength photons are absorbed more efficiently. Consequently, the stable and higher value of J_{SC} was detected at the reduced thickness. When the thickness of the PSC increases, its bandgap becomes smaller. This change allows the material to absorb longer-wavelength light more adequately, thereby generating more electron-hole pairs. With the thickness surpassing the charge diffusion length, J_{SC} either reaches a saturation point or decreases owing to the recombination of charge carriers.[44] Regarding the fill factor (FF), it exhibited a decreasing trend because of the increase in series resistance with increasing absorber layer thickness[45] which can also be explained by following the Eqs. (9) and (10).[24]

$$\boldsymbol{r} = \frac{\boldsymbol{\rho b}}{\boldsymbol{a}^2} \tag{9}$$

$$\boldsymbol{R}_s \cong \boldsymbol{\rho b} + \frac{\boldsymbol{\rho}_s \boldsymbol{L}^2}{2} \tag{10}$$

Table IV The initial physical parameters of ETL, absorber layer, and HTL were used to calculate the optimized device parameters

Parameters	FTO	ZnO	ZnOS	$Cs_2AgBi_{1-x}Sb_xBr_6$	Cu_xO
Thickness, t (nm)	500	70	70	400	350
Bandgap, E_g (eV)	3.5	3.3	2.83	1.8	2.17 (varied)
Electron affinity, χ (eV)	4.00	4.00	3.6	3.58	3.2
Dielectric permittivity, ε_r	9.00	9.0	9.0	6.5	7.1
CB effective density of states, N_c (cm^{-3})	2.2×10^{18}	3.7×10^{18}	2.2×10^{18}	2.2×10^{18}	2.02×10^{17}
VB effective density of states, N_v (cm^{-3})	1.8×10^{19}	1.8×10^{19}	1.8×10^{18}	1.8×10^{19}	1.10×10^{19}
Electron thermal velocity, V_e (cm/s)	1×10^7	1×10^7	1×10^7	1×10^7	1×10^7
Hole thermal velocity, V_h (cm/s)	1×10^7	1×10^7	1×10^7	1×10^7	1×10^7
Electron mobility, μ_e (cm^2/V s)	20	100	100	2	200 (varied)
Hole mobility, μ_h (cm^2/V s)	10	25	25.0	2	80
Shallow uniform acceptor density, N_A (cm^{-3})	0	0	0	1×10^{17}	9×10^{21}
Shallow uniform donor density, N_D (cm^{-3})	1×10^{18}	5×10^{17}	2×10^{18}	1×10^{13}	0
Defect density,‘$_t$ (cm^{-3})	1×10^{15}	1×10^{15}	1×10^{15}	1×10^{14}	1×10^{14}
References	38	39	40	41	42

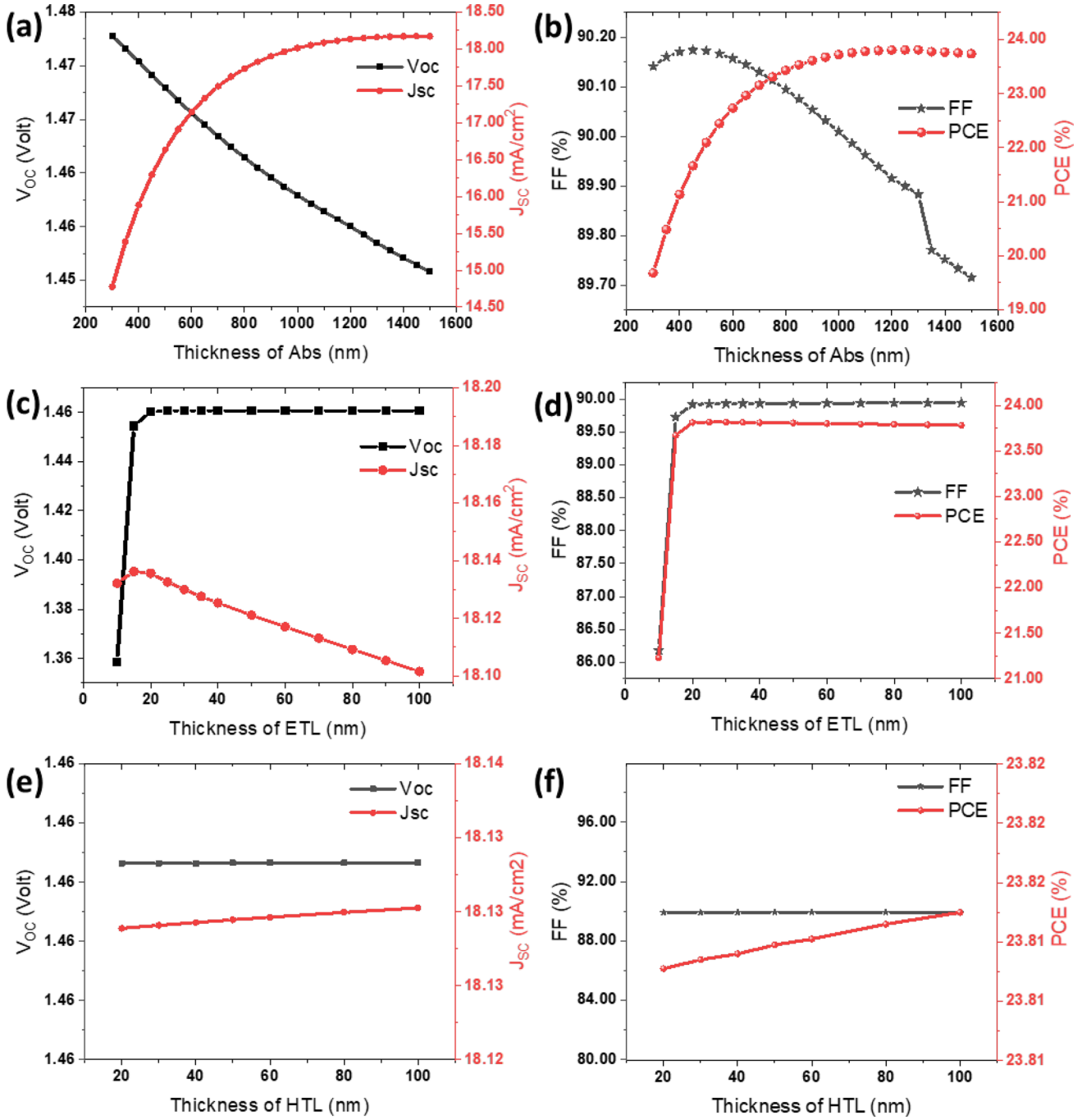

Fig. 6 The variation in photovoltaic parameters with respect to the thickness of the light-harvesting layer, ETL, and HTL includes the following aspects: (a, c, e) V_{OC} and J_{SC} (b, d, f), FF and PCE, respectively.

where ρ_s denotes sheet resistance, R_s denotes series resistance, r represents the internal resistance of light-harvesting layer, a represents base area, b represents thickness of the light-harvesting layer, L represents length, and ρ represents the resistivity of the absorber layer. V_b

The decrease in V_{OC} occurred owing to the decrease in dark saturation current as the absorber layer's thickness increased.[46] Another critical parameter, the power conversion efficiency (PCE), also improved with increased thickness. The PCE of the cell climbed from 19.68% to 23.74% as the thickness was adjusted from 300 nm to 1500 nm. With the thickness being reduced, reduction in the light absorption occurs, leading to low photogeneration which eventually results in lower efficiency. With the increase in thickness,

efficiency reaches saturation due to the saturation of light absorption and the open-circuit current density. Beyond 1150 nm, minimal changes in all photovoltaic parameters are apparent. This might be because the absorber layer is considerably larger than the diffusion lengths.[47] Therefore, 1200 nm was determined to be the optimal thickness for the absorber layer. At this optimal thickness, the photovoltaic parameters V_{OC}, J_{SC}, FF, and PCE were estimated to be 1.46 V, 18.1131 mA/cm^2, 89.94%, and 23.80%, respectively.

The accurate choice of parameters for ETL and HTL is vital in crafting highly efficient solar cells. Carefully selecting the ETL reduces recombination current and greatly amplifies transmittance, resulting in remarkably enhanced overall performance. The impact of varying the ETL thickness from 10 nm to 100 nm was explored on the solar cell's performance parameters. During this study, the thicknesses of the HTL and the perovskite layer were maintained at 50 nm and 1150 nm, respectively. The output parameters V_{OC}, PCE, and FF experienced a rise in their values nonetheless, J_{SC} remained almost unaffected by the change in thickness of the ETL layer. As an optimal thickness for the ETL layer, 25 nm was selected because after 25 nm, the photovoltaic parameters V_{OC}, FF, and PCE reached a saturation point. Similarly, alterations in the HTL thickness led to minimal changes in photovoltaic parameters, indicating that HTL thickness has little effect on device performance. Based on practical considerations and data analysis, 50 nm was the optimal HTL thickness.

The energy band alignment between the layers of the ZnOS/$Cs_2AgBi_{1-x}Sb_xBr_6$/CuxO solar cell structure (shown in Fig. 7) plays a critical role in determining the charge carrier dynamics and overall device performance. The halide double-perovskite absorber layer, $Cs_2AgBi_{1-x}Sb_xBr_6$, possesses a bandgap of approximately 1.8–2.1 eV, with a valence band maximum (VBM) near −5.38 eV and conduction band minimum (CBM) around −3.58 eV. Upon Sb incorporation, the VBM slightly increases, which is favorable for hole extraction. The Cu_xO layer (Cu_2O:CuO), exhibits a higher VBM (−5.37 eV) than the absorber, facilitating efficient hole transfer from the perovskite to the hole transport layer (HTL). Additionally, the downward CBM offset between $Cs_2AgBi_{1-x}Sb_xBr_6$ and Cu_xO forms a type II band alignment that effectively suppresses electron backflow and minimizes recombination losses at the interface. Meanwhile, the ZnOS electron transport layer (ETL) aligns well with the CBM of the absorber serves as an efficient hole-blocking layer, promoting selective electron extraction. Collectively, the band structure of this device configuration supports efficient charge separation and transport, with the Cu_xO HTL showing excellent energy level compatibility for effective hole extraction from the $Cs_2AgBi_{1-x}Sb_xBr_6$ absorber.

Influence of Defect Density on Quantum Efficiency

The bulk defect density of the light-absorbing layer was adjusted between 10^{11} cm^{-3} and 10^{17} cm^{-3} to explain the effects of varying bulk defect density on quantum efficiency (QE). The outcomes are depicted in Fig. 8a. For defect densities of 10^{11} cm^{-3}, 10^{12} cm^{-3}, and 10^{13} cm^{-3}, QE of approximately 100% was noted for light wavelengths ranging from 360 nm to 450 nm. Minimal differences were observed for bulk defect densities of 10^{11} cm^{-3}, 10^{12} cm^{-3}, 10^{13} cm^{-3}, and 10^{13} cm.$^{-3}$ However, a notable change was detected at defect densities of 10^{15} cm^{-3}, 10^{16} cm^{-3}, and 10^{17} cm^{-3}. As the bulk defect density increased, a corresponding decrease in QE was evident. QE remained largely consistent across all densities between 360 nm and 680 nm. After 680 nm, no visible changes in QE were observed. The QE values were

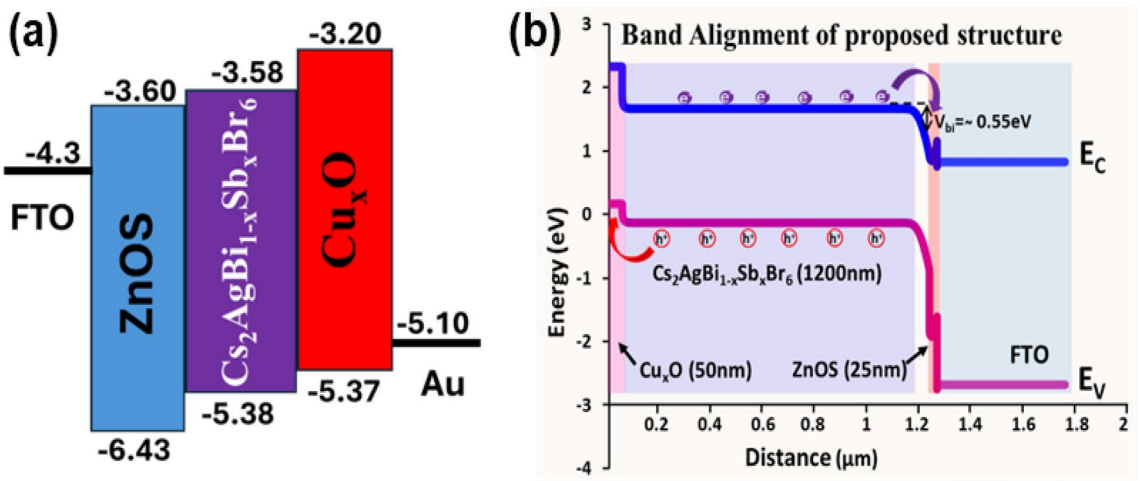

Fig. 7 (a) Schematic diagram of VBM and CBM and (b) band alignment of the FTO/ZnOS/Cs2AgBi1$_{-x}$SbxBr6/CuxO device structure observed in this work.

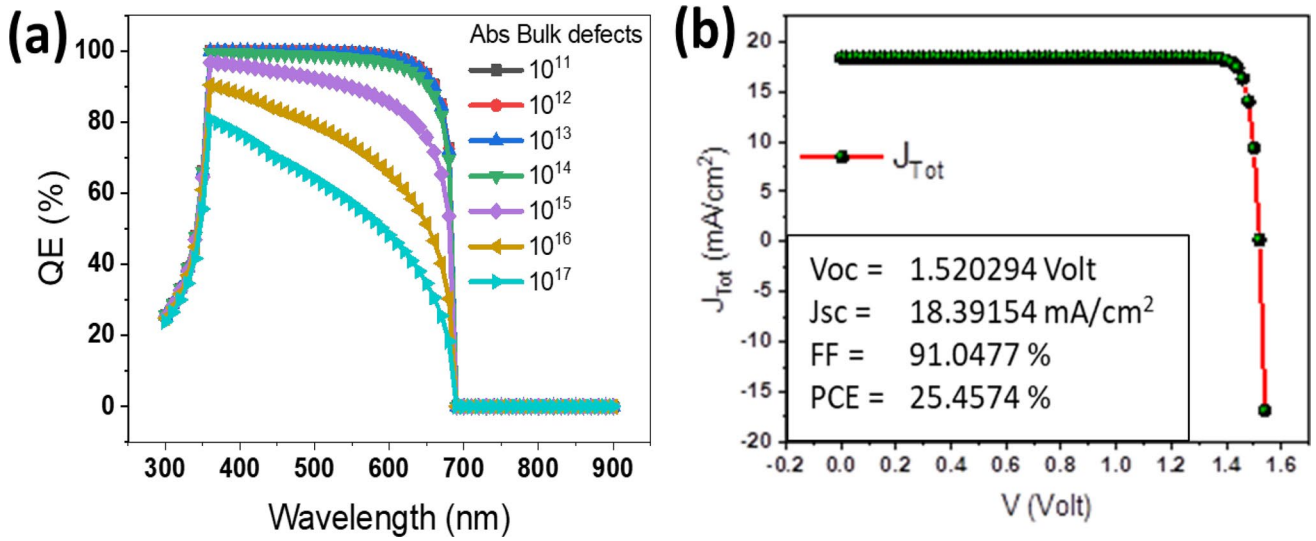

Fig. 8 (a) Impact of bulk defect density on quantum efficiency and (b) optimized current-voltage curve.

100% at a wavelength of 400 nm and 72% at 680 nm, for the simulated structure with a bulk defect density of 10^{13} cm^{-3}. A greater accumulation of charge carriers has been indicated through the higher QE values, emphasizing the outstanding performance of the simulated structure, especially under visible light conditions.[48]

The overall simulated photoconversion efficiency was calculated after thickness and other defect optimization (bulk defect and interface defect) and using the experimental values of Cu_xO thin films. Figure 8 presents the optimized J-V characteristic curve for the optimized PSC, with the inset displaying the relevant characteristic parameters. The optimized IV curve analysis reveals key photovoltaic parameters: $V_{OC} = 1.52$ V, $J_{SC} = 18.39$ mA cm^{-2}, FF = 89.88%. These photovoltaic parameters collectively result in the optimized and experimental values of Cu_xO thin films proposed PSCs achieving a maximum PCE of up to 25.46 %. This results comparatively highest among the all reported PCE as per our knowledge which is depicted in the following Table V.

It must be mentioned that the SCAPS-1D simulations were conducted in partially idealized input parameters, including high mobility of holes and low defect concentrations from literature benchmarks and measured values. These are the conditions under which the potential performance of the proposed device structure is estimated; however, in reality, experimental efficiencies may be lower due to actual conditions such as interface recombination, material inhomogeneity, and higher defect concentrations. Accordingly, the simulated results have to be treated as optimistic forecasts for the purpose of guiding future experimental activity.

Conclusion

This paper demonstrates a straightforward and scalable method of synthesizing high-quality Cu_xO thin films through the oxidation of CuI layers that have been processed from solution. The process enables the formation of good-quality mixed Cu_2O/CuO phases with good optoelectronic properties, including suitable bandgaps (1.65–2.20 eV), and high visible absorption. Compared to conventional HTLs such as Spiro-OMeTAD (~10^{-4}–10^{-3} cm^2 V^{-1} s^{-1}, undoped) and

Table V $Cs_2AgBi_{1-x}Sb_xBr_6$ -based solar cell photovoltaic properties

Device structure	V_{OC} (V)	*Jsc* (mA/ cm^2)	*FF* (%)	η (%)	References
PCBM/$Cs_2AgBi_{0.6}Sb_{0.4}Br_6$/NiOx (Experimental)	0.28	1.07	31	0.09	49
mpTiO$_2$/$Cs_2AgBi_{0.75}Sb_{0.25}Br_6$/PTAA/Au (Experimental)	0.59	0.94	51	0.28	50
NiO/$Cs_2AgBi_{0.75}Sb_{0.25}Br_6$/PCBM/$SnO_2$ (Simulation)	1.14	14.9	58.70	10.01	41
SpiroOMeTAD/ $Cs_2AgBi_{0.75}Sb_{0.25}Br_6$/ PCBM/ZnO (Simulation)	1.13	15.55	58.46	10.32	51
ZnOS/$Cs_2AgBi_{0.75}Sb_{0.25}Br_6$(400 nm)/$Cu_2O$ (Simulation)	1.39	16.04	78.34	18.18	34
ZnOS/$Cs_2AgBi_{1-x}Sb_xBr_6$(400 nm)/Cu_2O (Experimental + simulation)	1.52	18.39	89.88	25.46	This work

PEDOT:PSS (~0.1–1 $cm^2 V^{-1} s^{-1}$), Cu_xO offers significantly enhanced hole mobility, enabling efficient charge extraction and reduced recombination losses. Structural and electrical analyses indicate that film quality significantly enhances under optimized coating and annealing conditions. Numerical simulations with realistic material parameters obtained from the measured films predict that the optimized Cu_xO HTL should be able to maintain power conversion efficiencies above 25 % in idealized lead-free $Cs_2AgBi_{1-x}Sb_xBr_6$ perovskite solar cells. While these predictions are based on modeled architectures and optimal input parameters, they provide a strong motivation towards subsequent experimental verification. The inorganic nature and high hole mobility of Cu_xO make it suitable for use in devices where thermal and chemical stability are critical, such as ambient-processed Sn-based perovskites ($MASnI_3$ and $FASnI_3$) prone to oxidation. This work presents a versatile, low-temperature-processable, and thermally stable HTL strategy compatible with a broad range of lead-free perovskites, thereby advancing the development of environmentally friendly, non-toxic, and cost-effective perovskite solar cells.

Acknowledgments This work was supported by the Malaysian Ministry of Higher Education through FRGS grant FRGS/1/2020/TK0/UM/02/33. The authors also acknowledge the support from the Faculty of Engineering, Universiti Malaya (UM), and the School of Science, Edith Cowan University, Australia.

Author contributions Md. Jakir Hossen, Mohammad Aminul Islam, Mohammad Nur-E-Alam: Writing—review and editing, Writing—original draft, Visualization, Validation, Methodology, Investigation, Formal analysis, Data curation, Conceptualization. Md. Shahinuzzaman, MS Jamal, Suhana Mohd Said, S F W M Hatta, Md. Helal Miah, Mayeen Uddin Khandaker: Visualization, Validation, Formal analysis, Data curation. Mohammad Aminul Islam: Supervision. All the authors have read and agreed to the published version of the manuscript.

Funding Open Access funding enabled and organized by CAUL and its Member Institutions. Ministry of Higher Education, Malaysia, FRGS/1/2020/TK0/UM/02/33.

Data availability Data will be available on request.

Conflict of interest The authors declare no conflicts of interest.

Open Access This article is licensed under a Creative Commons Attribution 4.0 International License, which permits use, sharing, adaptation, distribution and reproduction in any medium or format, as long as you give appropriate credit to the original author(s) and the source, provide a link to the Creative Commons licence, and indicate if changes were made. The images or other third party material in this article are included in the article's Creative Commons licence, unless indicated otherwise in a credit line to the material. If material is not included in the article's Creative Commons licence and your intended use is not permitted by statutory regulation or exceeds the permitted use, you will need to obtain permission directly from the copyright holder. To view a copy of this licence, visit http://creativecommons.org/licenses/by/4.0/.

References

1. N. Renewable Energy Laboratory, "NREL Best Research-Cell PV Efficiency Chart," 2025.
2. O. Malinkiewicz et al., Perovskite solar cells employing organic charge-transport layers. *Nat. Photonics* 8(2), 128–132 (2014). https://doi.org/10.1038/nphoton.2013.341.
3. H. Zhou, "Interface engineering of highly efficient perovskite solar cells," *Science (1979)*, vol. 345, no. 6196, pp. 542–546, 2014.
4. P. Qin, "Inorganicholeconductor-basedleadhalide perovskitesolarcellswith12.4%conversion efficiency," *Nat Commun*, vol. 3834, no. 5, 2014.
5. K. C. Wang *et al.*, "P-type mesoscopic nickel oxide/organometallic perovskite heterojunction solar cells," *Sci Rep*, vol. 4, Apr. 2014, https://doi.org/10.1038/srep04756.
6. S. Ye et al., CuSCN-Based Inverted Planar Perovskite Solar Cell with an Average PCE of 15.6%. *Nano Lett.* 15(6), 3723–3728 (2015). https://doi.org/10.1021/acs.nanolett.5b00116.
7. J.A. Christians, R.C.M. Fung, and P.V. Kamat, An inorganic hole conductor for Organo-lead halide perovskite solar cells. improved hole conductivity with copper iodide. *J. Am. Chem. Soc.* 136(2), 758–764 (2014). https://doi.org/10.1021/ja411014k.
8. T. Jiang et al., Photoinduced charge transfer in ZnO/Cu2O heterostructure films studied by surface photovoltage technique. *Phys. Chem. Chem. Phys.* 12(47), 15476–15481 (2010). https://doi.org/10.1039/c0cp01228a.
9. C. Zuo, and L. Ding, Solution-Processed Cu2O and CuO as Hole Transport Materials for Efficient Perovskite Solar Cells. *Small* 11(41), 5528–5532 (2015). https://doi.org/10.1002/smll.201501330.
10. M. A. Islam *et al.*, "High mobility reactive sputtered CuxO thin film for highly efficient and stable perovskite solar cells," *Crystals (Basel)*, vol. 11, no. 4, Apr. 2021, https://doi.org/10.3390/cryst11040389.
11. C. Lin *et al.*, "The Investigation of the Influence of a Cu2O Buffer Layer on Hole Transport Layers in MAPbI3-Based Perovskite Solar Cells" *Materials*, vol. 15, no. 22, Nov. 2022, https://doi.org/10.3390/ma15228142.
12. S. Chatterjee, and A.J. Pal, Introducing Cu2O thin films as a hole-transport layer in efficient planar perovskite solar cell structures. *J. Phys. Chem. C* 120(3), 1428–1437 (2016). https://doi.org/10.1021/acs.jpcc.5b11540.
13. S. Joseph, and P.V. Kamath, Electrochemical deposition of Cu2O on stainless steel substrates: Promotion and suppression of oriented crystallization. *Solid State Sci.* 10(9), 1215–1221 (2008). https://doi.org/10.1016/j.solidstatesciences.2007.11.007.
14. L. C. Chen, C. C. Wang, and S. W. Lu, "Annealing effects of sputtered Cu2O nanocolumns on ZnO-coated glass substrate for solar cell applications," *J Nanomater*, vol. 2013, 2013, https://doi.org/10.1155/2013/891365.
15. G. Jimenez-Cadena, E. Comini, M. Ferroni, and G. Sberveglieri, Synthesis of Cu2O bi-pyramids by reduction of Cu(OH)2 in solution. *Mater. Lett.* 64(3), 469–471 (2010). https://doi.org/10.1016/j.matlet.2009.11.051.
16. R. Nordseth, R. Kumar, K. Bergum, I. Chilibon, S. E. Foss and E. Monakhov, "Nitrogen-doped Cu2O thin films for photovoltaic applications," *Materials*, vol. 12, no. 18, Sep. 2019, https://doi.org/10.3390/ma12183038.
17. D. Suriyani and C. Halin, "CHARACTERIZATION OF CUPROUS OXIDE THIN FILMS ON n-Si SUBSTRATE PREPARED BY SOL-GEL SPIN COATING," 2008. [Online]. Available: https://www.researchgate.net/publication/261296097

18. W. Nie, "Solar cells. 2015 High-efficiency solution-processed perovskite solar cells with millimeter-scale grains," *Science,* 347, 6221, pp. 522–525
19. J. Kim, Effect of defects on reaction of NiO surface with Pb-contained solution. *Sci. Rep.* 7, 44805 (2017). https://doi.org/10.1038/srep44805.
20. W. Sun et al., High-performance inverted planar heterojunction perovskite solar cells based on a solution-processed CuOx hole transport layer. *Nanoscale* 8(20), 10806–10813 (2016). https://doi.org/10.1039/c6nr01927g.
21. M. Jakir Hossen et al., Recent progress on the efficiency and stability of lead-free $Cs_2AgBiBr_6$ double halide perovskite solar cells. *Inst. Phys.* (2025). https://doi.org/10.1088/1402-4896/ad9b59.
22. K.Z. Du, W. Meng, X. Wang, Y. Yan and D.B. Mitzi, Bandgap engineering of lead-free double perovskite $Cs_2AgBiBr_6$ through trivalent metal alloying. *Angewandte Chemie Int. Edition* 56(28), 8158–8162 (2017). https://doi.org/10.1002/anie.201703970.
23. Y. Liu et al., Bandgap-tunable double-perovskite thin films by solution processing. *Mater. Today* 28, 25–30 (2019). https://doi.org/10.1016/j.mattod.2019.04.023.
24. M.J. Hossen et al., Modeling and optimization of high efficiency Pb-free Cs-based halide double perovskite solar cell using SCAPS-1D. *J. Opt. (India)* (2025). https://doi.org/10.1007/s12596-025-02550-9.
25. N. Serin, T. Serin, Ş Horzum and Y. Çelik, Annealing effects on the properties of copper oxide thin films prepared by chemical deposition. *Semicond. Sci. Technol.* 20(5), 398–401 (2005). https://doi.org/10.1088/0268-1242/20/5/012.
26. J. Naktiyok and A. K. Özer, "BAKIR ASETAT MONOHİDRATIN (Cu(CH3COO)2.H2O) TERMAL BOZUNMASINDAN BAKIR OKSİT (CuO) SENTEZİ," *Ömer Halisdemir Üniversitesi Mühendislik Bilimleri Dergisi*, Jul. 2019, https://doi.org/10.28948/ngumuh.598177.
27. A. Hannan, S. Islam, S.R. Parvin, and J. Hossen, Unusual crystal-lattice behaviour of CeSb at ambient pressure. *J. Natl. Sci. Foundation Sri Lanka* 38(3), 201–205 (2010).
28. A. Rydosz, K. Dyndał, W. Andrysiewicz, D. Grochala and K. Marszałek, GLAD magnetron sputtered ultra-thin copper oxide films for gas-sensing application. *Coatings* (2020). https://doi.org/10.3390/coatings10040378.
29. B. Balamurugan and B.R. Mehta, "Optical and structural properties of nanocrystalline copper oxide thin films prepared by activated reactive evaporation. *Thin Solid Films* 396(1–2), 90–96 (2001).
30. M.R. Johan, M.S.M. Suan, N.L. Hawari and H.A. Ching, Annealing effects on the properties of copper oxide thin films prepared by chemical deposition. *Int. J. Electrochem. Sci.* 6(12), 6094–6104 (2011). https://doi.org/10.1016/s1452-3981(23)19665-9.
31. H. Rahal, R. Kihal, A.M. Affoune and S. Rahal, Electrodeposition and characterization of Cu_2O thin films using sodium thiosulfate as an additive for photovoltaic solar cells. *Chin. J. Chem. Eng.* 26(2), 421–427 (2018). https://doi.org/10.1016/j.cjche.2017.06.023.
32. C. Malerba, F. Biccari, C.L. Azanza Ricardo, M. Dincau, P. Scardi and A. Mittiga, "Erratum: absorption coefficient of bulk and thin film Cu_2O. *Solar Energy Mater. Solar Cells* 95(10), 2848–2854 (2012). https://doi.org/10.1016/j.solmat.2011.10.018.
33. P. Pattanasattayavong, S. Thomas, G. Adamopoulos, M.A. McLachlan and T.D. Anthopoulos, P-channel thin-film transistors based on spray-coated Cu2O films. *Appl. Phys. Lett.* 102, 16 (2013). https://doi.org/10.1063/1.4803085.
34. N. Singh, A. Agarwal and M. Agarwal, Performance evaluation of lead–free double-perovskite solar cell. *Opt Mater (Amst)* 114, 1–11 (2021). https://doi.org/10.1016/j.optmat.2021.110964.
35. M. Burgelman, K. Decock, A. Niemegeers, J. Verschraegen, and S. Degrave, "SCAPS manual."
36. S. Zandi, P. Saxena, M. Razaghi and N.E. Gorji, Simulation of CZTSSe thin-film solar cells in COMSOL: three-dimensional optical, electrical, and thermal models. *IEEE J. Photovolt.* 10(5), 1503–1507 (2020). https://doi.org/10.1109/JPHOTOV.2020.2999881.
37. M. Kumar, A. Kumar, A. Raj, P. C. Sati, M. Sahni and A. Anshul, "Organic-inorganic perovskite-based solar cell designs for high conversion efficiency: A comparative study by SCAPS simulation," in *Materials Today: Proceedings*, Elsevier Ltd, 2020, pp. 3081–3087. https://doi.org/10.1016/j.matpr.2020.11.035.
38. U. Mandadapu, Simulation and analysis of lead based perovskite solar cell using SCAPS-1D. *Indian J. Sci. Technol.* 10(1), 1–8 (2017). https://doi.org/10.17485/ijst/2017/v11i10/110721.
39. D. Jalalian, A. Ghadimi and A. Kiani, Modeling of a high performance bandgap graded Pb-free HTM-free perovskite solar cell. *Eur. Phys. J. Appl. Phys.* 87(1), 10101 (2019). https://doi.org/10.1051/epjap/2019190095.
40. S. I. Rahman, S. Faisal, S. Ahmed and T. I. Dhrubo, "A comparative study on different HTMs in perovskite solar cell with ZnOS electron transport layer," in *5th IEEE Region 10 Humanitarian Technology Conference 2017, R10-HTC 2017*, Institute of Electrical and Electronics Engineers Inc., Feb. 2018, pp. 546–550. https://doi.org/10.1109/R10-HTC.2017.8289019.
41. J. Madan, R. Pandey and R. Sharma, Device simulation of 17.3% efficient lead-free all-perovskite tandem solar cell. *Sol. Energy* 197, 212–221 (2020). https://doi.org/10.1016/j.solener.2020.01.006.
42. M.I. Hossain, F.H. Alharbi and N. Tabet, Copper oxide as inorganic hole transport material for lead halide perovskite based solar cells. *Sol. Energy* 120, 370–380 (2015). https://doi.org/10.1016/j.solener.2015.07.040.
43. H.R. Arzbin and A. Ghadimi, Improving the performance of a multi-junction solar cell by optimizing BSF, base and emitter layers. *Mater. Sci. Eng. B* 243, 108–114 (2019). https://doi.org/10.1016/j.mseb.2019.04.001.
44. F. Jannat, S. Ahmed and M.A. Alim, Performance analysis of cesium formamidinium lead mixed halide based perovskite solar cell with MoOx as hole transport material via SCAPS-1D. *Optik (Stuttg)* (2021). https://doi.org/10.1016/j.ijleo.2020.166202.
45. W. Abdelaziz, A. Shaker, M. Abouelatta and A. Zekry, Possible efficiency boosting of non-fullerene acceptor solar cell using device simulation. *Opt Mater (Amst)* 91, 239–245 (2019). https://doi.org/10.1016/j.optmat.2019.03.023.
46. A. Zekry, A. Shaker and M. Salem, "Solar cells and arrays: principles, analysis, and design," in *Advances in Renewable Energies and Power Technologies: Volume 1: Solar and Wind Energies*, vol. 1, Elsevier, 2018, pp. 3–56. https://doi.org/10.1016/B978-0-12-812959-3.00001-0.
47. J.P. Correa-Baena et al., Unbroken perovskite: interplay of morphology, electro-optical properties, and ionic movement. *Adv. Mater.* 28(25), 5031–5037 (2016). https://doi.org/10.1002/adma.201600624.
48. M.B. Rahman, N. Noor-E-Ashrafi, M.H. Miah, M.U. Khandaker and M.A. Islam, Selection of a compatible electron transport layer and hole transport layer for the mixed perovskite FA0.85Cs0.15Pb (I0.85Br 0.15)3, towards achieving novel structure and high-efficiency perovskite solar cells: a detailed numerical study by SCAPS-1D. *RSC Adv.* 13(25), 17130–17142 (2023). https://doi.org/10.1039/d3ra02170j.
49. A. Kumar, S.K. Swami, S.S. Rawat, V.N. Singh, O.P. Sinha and R. Srivastava, Mixed bismuth-antimony-based double perovskite nanocrystals for solar cell application. *Int. J. Energy Res.* 45(11), 16769–16780 (2021). https://doi.org/10.1002/er.6924.

50. M. Pantaler, S. Olthof, K. Meerholz and D.C. Lupascu, Bismuth-antimony mixed double perovskites Cs2AgBi1-xSbxBr 6 in solar cells. *MRS Adv.* 357, 1–8 (2019). https://doi.org/10.1557/adv.2019.404.
51. M. M. H. M. S. R. M. A. M. H. Asif Hossain, Fully lead-free all perovskite tandem solar cell with improved efficiency: device simulation using S*CAPS-1D*. IEEE, 2020. doi.org/https://doi.org/10.1109/TENSYMP50017.2020.9230927.

Publisher's Note Springer Nature remains neutral with regard to jurisdictional claims in published maps and institutional affiliations.